Quasiparticle and superfluid dynamics in Magic-Angle Graphene

Elías Portolés [1] ✉, Marta Perego[1], Pavel A. Volkov [2,3] ✉, Mathilde Toschini[1], Yana Kemna[1], Alexandra Mestre-Torà [1], Giulia Zheng [1], Artem O. Denisov [1], Folkert K. de Vries[1], Peter Rickhaus[1], Takashi Taniguchi [4], Kenji Watanabe [5], J. H. Pixley [6,7], Thomas Ihn [1,8] & Klaus Ensslin [1,8]

Magic-Angle Twisted Bilayer Graphene (MATBG) shows a wide range of correlated phases which are electrostatically tunable. Despite a growing knowledge of the material, there is yet no consensus on the microscopic mechanisms driving its superconducting phase. A major obstacle to progress in this direction is that key thermodynamic properties, such as specific heat, electron-phonon coupling and superfluid stiffness, are challenging to measure due to the 2D nature of the material and its relatively low energy scales. Here, we use a gate-defined, radio frequency-biased, Josephson junction to probe the electronic dynamics of MATBG. We demonstrate evidence for two processes determining the low-frequency dynamics across the phase diagram: thermalization of electronic quasiparticles through phonon scattering and inductive response of the superconducting condensate. A phenomenological approach allows us to relate the experimentally observed dynamics to several thermodynamic properties of MATBG, including electron-phonon coupling and superfluid stiffness. Our findings support anisotropic or nodal superconductivity in MATBG and demonstrate a broadly applicable method for studying properties of 2D materials with out-of-equilibrium nanodevice dynamics.

Magic-angle twisted bilayer graphene (MATBG) is one of the most prominent examples of a two-dimensional strongly correlated material. It consists of two layers of graphene twisted with respect to each other by an angle of 1.1 degrees. In reciprocal space, this results in the hybridization of the Dirac cones of the different layers, leading to the so-called flat bands. When the Fermi energy of the material is tuned, through field-effect, to such bands, electron-electron correlations determine the electronic state of the material. This results in a phase diagram[1,2] that has drawn considerable attention due to the presence of insulating, topological and superconducting phases[3]. The

combination of superconductivity and field-effect tunability make it a promising platform for versatile superconducting electronics.

Despite these remarkable discoveries, several questions remain open about the nature of the superconducting state and even less is understood about what is the driving mechanism behind it. The most central and pressing issues include whether the superconducting mechanism of MATBG is electronic or phonon-driven[4–7] and whether its superconducting gap is nodal or not[8,9]. Furthermore, the electron-phonon coupling has been suggested as the origin of the observed (putatively) universal linear-in-T resistance[4,10]. Characterizing the

[1]Laboratory for Solid State Physics, ETH Zurich, Zurich, Switzerland. [2]Department of Physics, University of Connecticut, Storrs, CT, USA. [3]Department of Physics, Harvard University, Cambridge, MA, USA. [4]Research Center for Materials Nanoarchitectonics, National Institute for Materials Science, Tsukuba, Japan. [5]Research Center for Electronic and Optical Materials, National Institute for Materials Science, Tsukuba, Japan. [6]Department of Physics and Astronomy, Center for Materials Theory, Rutgers University, Piscataway, NJ, USA. [7]Center for Computational Quantum Physics, Flatiron Institute, New York, NY, USA. [8]Quantum Center, ETH Zurich, Zurich, Switzerland. ✉e-mail: eliaspo@phys.ethz.ch; pavel.volkov@uconn.edu

electron-phonon coupling and the anisotropy of the superconducting gap is the first step towards answering these questions. However, the 2D nature of MATBG, the small moiré Brillouin zone, and the relatively low energy scales make the use of many standard techniques for investigating bulk materials, such as calorimetry, angle-resolved photoemission spectroscopy (ARPES) or neutron scattering, challenging or impossible. Similar concerns are relevant for all 2D superconductors, where in many cases the mechanism and character of superconductivity also remain undetermined[11–14].

Superconducting mesoscopic devices have proven to be a useful characterization tool of the material they are built of[15–17]. In particular, Josephson junctions (JJs) have been used as a probe of electronic thermalization rates[17], and the superfluid density, through characterizing the kinetic inductance in thin-film devices[16]. In the case of MATBG, superconducting devices have already proven instrumental for probing the charge of the Cooper pairs[18,19], the long-range coherence of the superconducting condensate[19] and its orbital magnetic properties[20].

Here, we use a gate-defined Josephson junction (JJ) in MATBG[18,20,21] to extract electron-phonon coupling, thermodynamic, and superfluid properties of MATBG across its phase diagram. Biasing the junction with a combination of DC and AC currents we probe the dynamics of both the electronic quasiparticles and the superfluid of MATBG. We show that the measured timescales governing the junction's transition between resistive and superconducting states are directly related to the microscopic properties of the material, such as electronic cooling power due to phonons, specific heat, and superfluid density. The gate-tunability of the device allows us to probe these quantities across the density-tuned phase diagram of MATBG, for chemical potential both within and outside the flat bands. These measurements allow to constrain the electron-phonon coupling of MATBG, and the current bias dependence of the superfluid density is incompatible with isotropic pairing.

Our experimental setup and theoretical models can be applied to other two-dimensional materials, establishing a tool for the study of two-dimensional superconductors at cryogenic temperatures. They advance the state of the art for MATBG, directly probing the superfluid density, rather than spectroscopic[8] properties of the superconducting state. They also allow for the characterization of the thermal relaxation across the whole phase diagram of MATBG and at cryogenic temperatures. Previous studies either accessed only parts of the phase diagram [22] or were limited to higher temperatures[23], where correlation effects are suppressed[1,2].

Results
Overview
Our device is a JJ electrostatically defined in MATBG, with a twist angle of 1.06° ± 0.04°, also studied in reference[18] (Fig. 1a). The global carrier density n, tuned by the back gate, is set to $n = -1.73 \times 10^{-12}$ cm^{-2}, at which the bulk has its highest critical current, 250 nA (See SI). Two layers of top gates, separated by a layer of Al$_2$O$_3$, tune the local density in the central region, allowing us to fine-tune the details of the junction.

For each value of electron density in the central region (Fig. 1b) we analyze the current-voltage (I/V) characteristic. For densities in the central region close to $n_j = -2$ we observe a gradual onset of resistance above a critical current value, consistent with bulk superconductivity (see also discussion of Fig. 1f below). For all other densities, we universally observe a hysteretic I/V trace with two characteristic voltage jumps ΔV, as shown in Fig. 1c. The two jumps correspond to switching from the superconducting to the resistive state (increasing current bias, blue line) and retrapping back (decreasing current bias, blue dashed). Together with Shapiro step measurements[18] this indicates the formation of a weak superconducting link between the left and right parts of the device, where the weak link region can switch between resistive and superconducting states. From the band structure of

MATBG[2] (see inset of Fig. 1(d), for a schematic), the weak link region is expected to be metallic except for a narrow range of voltages placing the chemical potential into the gap between the flat and dispersive bands. Such assessment is consistent with the observation of a positive excess current, I_{ex},[24,25] in the resistive state of a large portion of the phase diagram (green curve in Fig. 1d). In analogy to conventional superconductors[17], the dynamic response of such metallic weak links should give access to the dynamics of the electronic quasiparticles and the superconducting condensate in MATBG. We probe the dynamics of our weak links by adding a small AC current component to the DC current flowing through the junction. Sweeping the frequency across three orders of magnitude (0.1–100 MHz), we focus on the changes in the I/V characteristics, as shown in Fig. 1e. At low frequencies, the AC drive brings the two hysteresis branches closer together, which can be understood as follows. The abrupt character of switching and retrapping with DC bias suggests that the junction will undergo a change whenever the total current $I_{DC} + I_{RF}(t)$ reaches the critical value for switching (I_{sw}) or retrapping (I_{re}). Consequently, one expects the switching to occur prematurely at $I_{sw} - I_{RF}$, and the retrapping to occur at a higher DC bias, $I_{re} + I_{RF}$, reducing the size of the hysteresis loop.

For increasing frequency, the effect of AC bias gradually disappears (Fig. 1e), with a different rate for switching and retrapping. This indicates that both processes, in fact, do not occur instantaneously and are characterized each by a certain rate, which we denote as Γ_{re} and Γ_{sw}. We note that under switching (retrapping) rate we mean the characteristic scale for the switching (retrapping) current dependence on AC bias frequency, with a precise definition of that scale given below. At highest frequencies, the AC drive effect is absent, indicating that neither switching nor retrapping processes are fast enough to occur over one AC drive period. The switching and retrapping rates that can be extracted from Fig. 1e reflect the properties of superconducting MATBG. We now turn to their physical interpretation.

Modeling the weak link
We can first rule out switching and retrapping driven only by the dynamics of the superconducting phase difference across the junction, exemplified by, e.g., the Resistively and Capacitively Shunted Junction (RCSJ) model[24]. In that case, the characteristic frequency is fixed by the Josephson relation to $2e\Delta V/\hbar$. For our weak links it is of the order of 10 GHz, several orders of magnitude larger than the frequencies used in our experiments. The RCSJ model also predicts the switching rate to be smaller than the retrapping one, inconsistent with experimental observations (see additional discussion in Supplementary Information). We therefore conclude that our experimental observations require a mechanism beyond the RCSJ model to explain the switching and retrapping charateristics.

Such an alternative mechanism, for both the retrapping and the hysteresis in metallic weak links is the heating of the electrons in the junction, followed by their thermalization[17,26]. In this case the retrapping branch at $I < I_{sw}$ is characterized by a higher temperature than the switching one due to the Joule heating in the resistive state (Fig. 2a, b). This overheating reduces the weak link critical current for the retrapping branch, leading to a hysteresis. Most importantly, retrapping back into the superconducting state requires the electronic temperature to equilibrate to base temperature, a process, depicted in Fig. 2c, that has been directly demonstrated in superconductor-normal metal-superconductor junctions[17].

While there are several mechanisms for energy dissipation in graphene, at low temperatures the dominant one is the coupling between electrons and acoustic phonons. In particular, thermalization can occur via diffusion of hot electrons into the leads, emission of blackbody photons or interaction of electrons with acoustic phonons (as the optical ones are frozen out)[27]. The first mechanism is suppressed by the presence of a superconducting gap[28] in the leads in our case,
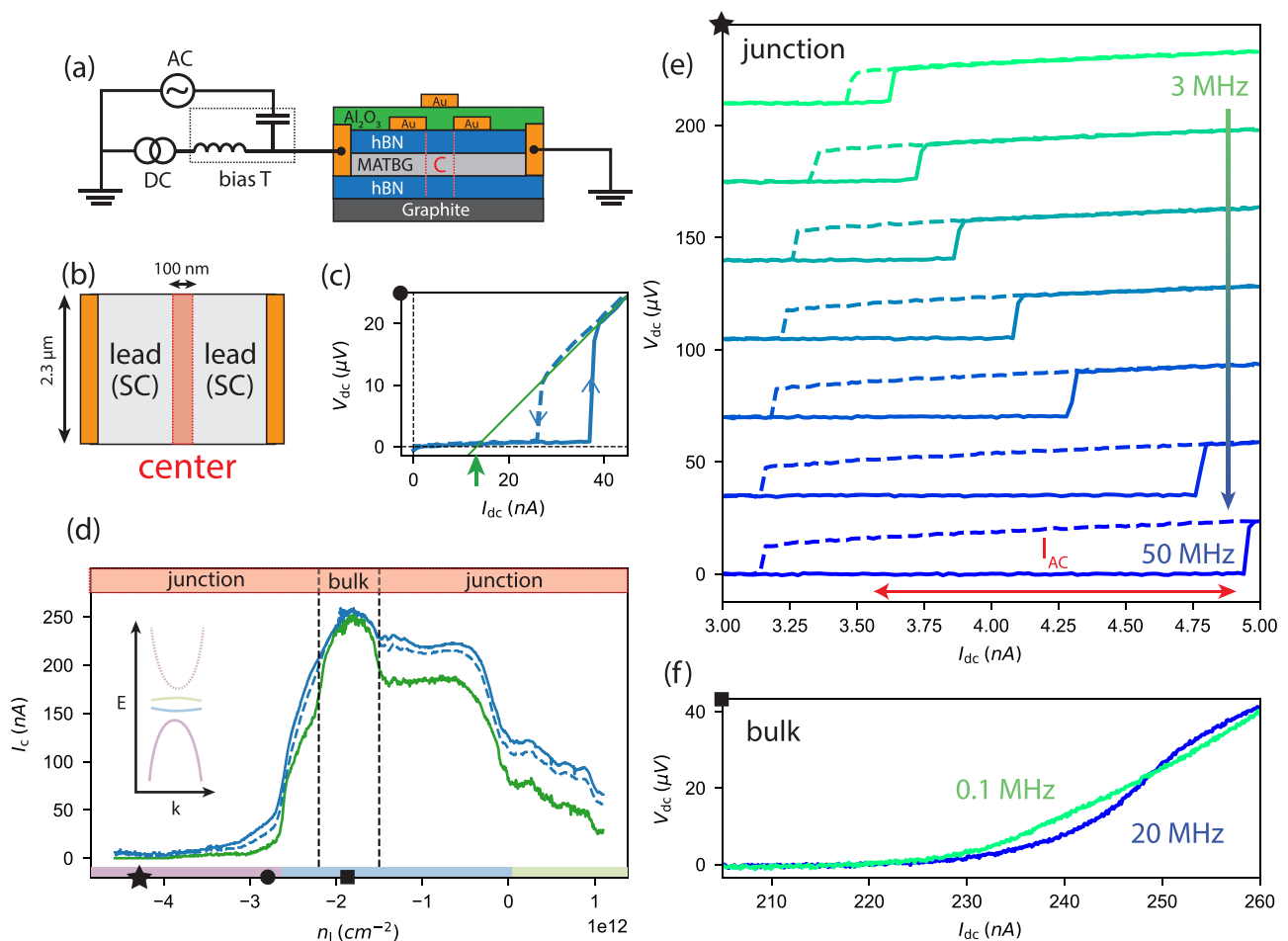
Fig. 1 | Device response to AC and DC biases. a Schematics of the device. The device is depicted by a cross section schematics. The vertical red dashed lines represent the central (C) region highlighted in (**b**). **b** Top-view simplified schematics with the gold contacts on the side, connected by a stripe of magic-angle twisted bilayer graphene (MATBG). The central region, of length 100 nm, is highlighted. The leads are superconducting (SC). **c** I/V characteristic of the junction at a density of -2.8×10^{12} cm^{-2}. In blue, solid line, a trace for increasing DC bias is shown. The dashed line represents the trace for decreasing bias. The green line is an extrapolation of the resistive part of the characteristic at 0 voltage. The green arrow highlights what is defined as excess current. **d** Switching (blue), retrapping (blue, dashed) and excess (green) currents as a function of density in the central region.

The colors on the x-axis correspond to the filling of the band structure schematics shown in the inset. The upper part indicates whether the I/V characteristic shows a junction-like or bulk superconductor-like behavior. The black star, circle and square indicate, respectively, the densities at which is taken the data shown in (**e**, **c**, **f**). **e** I/V traces of the junction for AC bias of increasing frequency and fixed amplitude (red arrow) as a function of DC bias (horizontal axis). Solid lines show positive bias directions while dashed ones show negative directions. Curves are offset vertically for readability. **f** I/V traces at bias AC amplitude 1.4 nA and frequencies of 0.1 MHz and 20 MHz when the sample is tuned to all-bulk configuration see panel (**d**).

while the second one has been estimated to be negligible in MATBG[29,30]. This suggests that the dominant heat loss mechanism is via coupling to phonons, in agreement with conventional SNS junctions[17,26].

The above mechanism on its own, however, still implies that switching occurs with the Josephson rate $2e\Delta V/\hbar$, which is inconsistent with our observations, as detailed above. To understand the switching dynamics in our devices we now turn to the case without a central gate voltage, i.e., where the sample is homogeneously superconducting at the optimal density. We observe a frequency-dependent IV characteristic (Fig. 1f), despite the absence of a weak link. Note that there is no hysteresis, ruling out overheating as its origin.

In addition to these observations, it has been shown that a supercurrent can flow in MATBG in narrow superconducting paths separated by normal regions[31]. The normal region thus forms a resistive shunt R_{bulk} coupled in parallel to the superconducting regions (purple shaded path in Fig. 2a). At a non-zero frequency ω, the superfluid impedance is purely inductive due to the inertia of the Cooper pairs (blue shaded mechanism in Fig. 2d) and given by $Z_{\mathrm{sc}} = j\omega L_{\mathrm{kin}}$, with the kinetic inductance $L_{\mathrm{kin}} \propto \frac{m^*}{n_s e^2}$, where m^* is the

effective mass, e the electron charge, and n_s is the superfluid density. At frequencies larger than $\frac{R_{\mathrm{bulk}}}{L_{\mathrm{kin}}}$, the impedance of the superconducting branch becomes higher than the resistance of the normal bulk and the AC current flows through the non-superconducting regions (purple shaded mechanism in Fig. 2d). Intriguingly, L_{kin} in MATBG is expected to be large[19] due to two unique properties: extremely low electron densities, and high effective mass[1]. This explains our observation of a rather low characteristic switching rate in Fig. 1f. The same mechanism applies for MATBG weak links - the kinetic inductance of bulk MATBG is then coupled in series to the junction (Fig. 2a).

Using the ideas outlined above, we construct a model to describe the non-equilibrium dynamics of the Josephson junction. Importantly, this model allows us to relate the observed switching and retrapping rates, Γ_{sw} and Γ_{re}, to the microscopic and thermodynamic properties of MATBG. The dynamics of the current-biased junction are described by:

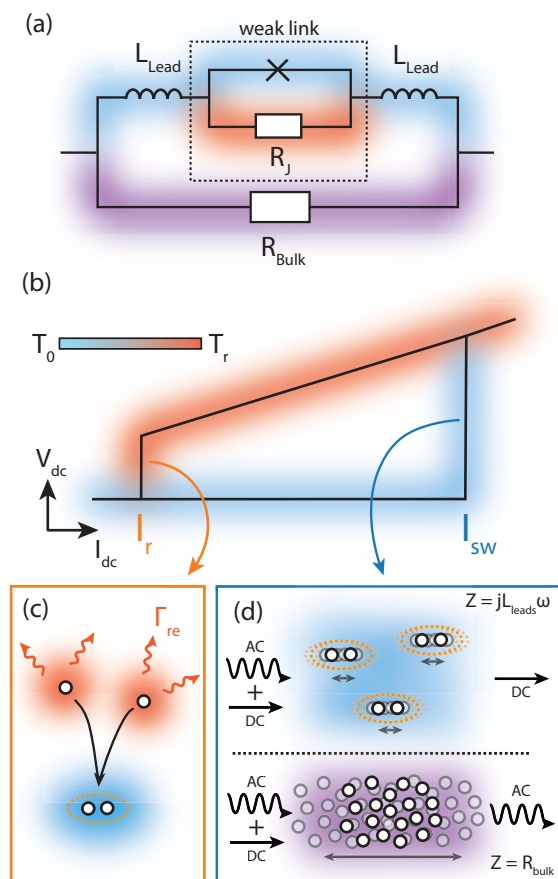$$I_{\mathrm{sc}}(t) - I_{\mathrm{ex}} = I_J(T)\sin(\varphi) + \frac{\hbar\dot{\varphi}}{2eR_J} \tag{1}$$

Fig. 2 | Model for the switching and retrapping mechanisms. a Equivalent scheme of the MATBG junction for densities inside the lower flat band: the weak-link region modelled as a resistively shunted junction is coupled in series with the kinetic inductance of the leads. The superconducting regions (blue and red) are further shunted by normal regions (purple). **b** Illustration of switching and retrapping mechanism and hysteresis origin in MATBG junctions. I_{re} and I_{sw} represent, respectively, the retrapping and switching currents. The retrapping branch of IV characteristic (red) is characterized by an increased electronic temperature T_r due to Joule heating, suppressing the critical current. Retrapping into the superconducting state requires cooling the electrons (**c**) to base temperature characterized by a rate dependent on electronic cooling power G_{th}. Switching rate (blue), on the other hand, is only limited by the shunting kinetic inductance of the bulk MATBG (**a**, **d**). **c** Electronic thermal relaxation in MATBG occurs via coupling to acoustic phonons. Two electronic quasiparticles in the junction release their thermal energy to the phonon bath and become cold enough to mediate Josephson coupling. This coupling is represented by an orange dashed line. Γ_{re} represents the thermalization rate. **d** Due to their inertia, Cooper pairs in a thin superconductor (blue region) prevent the transmission of RF signals at high frequencies. Instead, the AC current at frequencies above $\omega_L = \frac{R_{bulk}}{L_{leads}}$ is rerouted through non-superconducting regions of the sample (purple region) and does not affect the junction. Z represents the impedance seen by the signal, R_{bulk} the resistance of the bulk and L_{leads} the inductance of the leads.

$$C_{el}\dot{T} = \frac{1}{R_J}\left(\frac{\hbar\dot{\varphi}}{2e}\right)^2 - G_{th}T \qquad (2)$$

$$I(t) - I_{ex} = I_{sc} - I_{ex} + \frac{L_{kin}\dot{I}_{sc} + \frac{\hbar\dot{\varphi}}{2e}}{R_{bulk}} \qquad (3)$$

We highlight that this description has not been previously used to analyze either the MATBG[18,19,21] or conventional[17] Josephson junctions; in what follows below we show that it allows to describe the Josephson junction data in a self-contained way without invoking results of other measurements[29–31].

Equation (1) describes a Josephson junction with a phase difference φ, a temperature-dependent critical current $I_J(T)$, and a fixed excess current value I_{ex} shunted by resistance R_J (Fig. 2(a), dashed box). For results in the main text we assume $R_J \ll R_{bulk}$, the general case is discussed in Supplementary Information. We note that the form of $I_J(T)$ has not been determined experimentally; we assume that it is a decreasing function of temperature with a single characteristic scale T_J that can be estimated to be of the order 0.1 K based on the disappearance of interference in superconducting quantum interference devices (SQUIDs)[19]. In the main text, we focus on an empirical model $I_J = I_J(0)\sqrt{1 - T/T_J} \cdot \theta(1 - T/T_J)$ that correctly captures the high-frequency asymptotic behavior of the retrapping current; we provide a discussion of different models and their general properties in the Supplementary Information.

Equation (2) describes the evolution of the electronic temperature T with respect to the base temperature. The left-hand side represents the total power dissipated in the link, C_{el} being the electronic heat capacity. On the right-hand side, the first term corresponds to Joule heating, while the second one is the electronic heat loss (G_{th}) attributed, as discussed above, to electron-phonon interactions. The processes relevant for the description of the Josephson effect occur at $T \approx T_J$ (see Supplementary Information), such that the value of the thermal conductivity G_{th} can be approximated by its value at $T = T_J$. The final equation describes the shunting of the junction by the resistive quasiparticles of bulk MATBG (Fig. 2 (a,d)). The current $I_{sc}(t)$ is the full external current driven through the weak link.

Remarkably, we find that the model defined by Eq. (1)-(3) captures all of the behaviors observed in the experiment. As an example, we consider a highly nonlinear regime where the RF amplitude is larger than the hysteresis $I_{sw} - I_{re}$. For a range of DC bias values the junction spends part of the AC period in the resistive regime and part of it being superconducting, resulting in a double step in voltage, as shown in Fig. 3a. Such voltage values are the average between the resistive and superconducting voltages weighted by the percentage of the time spent by the junction in each regime. Fig. 3d shows a simulated trace in the same regime, demonstrating remarkable agreement between the model and the experiment. As we increase the frequency of the current bias across the junction we recover the regular hysteresis (Fig. 3a, b, black line). The model captures the evolution of the I/V traces as the bias frequency increases, as is shown in Fig. 3e. Even finer details of the experimental data, discussed in the Supplementary Information are captured by the model. These comparisons confirm that our model accurately describes the dynamics of our junction.

To extract the retrapping and switching rates, Γ_{re} and Γ_{sw}, for a given density from the experimental data, we fit the evolution of the retrapping and switching currents as a function of bias frequency. An analysis of the data, discussed in the Supplementary Information, demonstrates that both currents asymptotically approach a constant high-frequency value as $1/\omega$. To fit the results at all frequencies, we use the following functions: $I_{sw}(\omega) = I_{sw,\infty} - I_{RF}\Gamma_{sw}/\sqrt{\Gamma_{sw}^2 + \omega^2}$ and $I_{re}(\omega) = I_{re,\infty} + I_{RF}\Gamma_{re}/\sqrt{\Gamma_{re}^2 + \omega^2}$. That allows to characterize the corresponding rates (see Fig. 3(c), gray lines). The model described in Eqs. (1),(2),(3), reproduces correctly the asymptotic behavior of the switching current, while for the retrapping current the result depends on the particular form of $I_J(T)$ (see Supplementary Information). For a fixed density in the junction, we extract the switching and retrapping currents for all frequencies and fit the results. In the example shown in Fig. 3(c), for a density of $-4.5 \times 10^{12}\text{cm}^{-2}$, we extract $\Gamma_{re} = 0.52$ MHz and $\Gamma_{sw} = 2.75$ MHz. Therefore, the weak-link dynamics of our junction
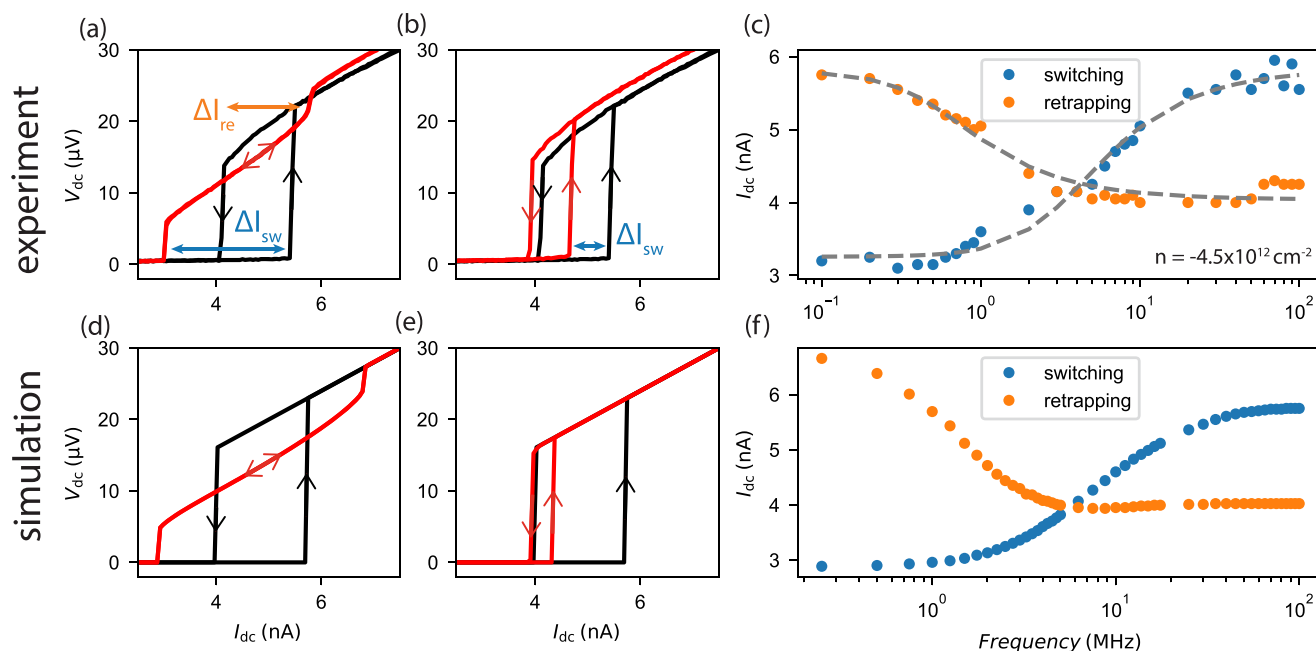
Fig. 3 | Extraction of the switching and rertapping rates. a I/V traces of the junction at bias frequencies of 0.1 MHz (red) and 100 MHz (black) in the regime where the effective AC amplitude is higher than the hysteresis. ΔI_{re} and ΔI_{sw} highlight the change in retrapping and switching currents, respectively, between the two bias frequencies. **b** I/V traces of the junction at bias frequencies of 8 MHz (red) and 100 MHz (black) in the regime where the effective AC amplitude is higher than the hysteresis. The mismatch in retrapping current between the red and black curves is probably due to a charge jump (note it is of the order of a few pA). **c** Switching and retrapping currents as a function of AC bias frequency. **d**–**f** Numerical simulations of our device in the same regime as the data shown in (**a**–**c**). The grey dashed line in (**c**) is a fit to the functional forms provided in equations (1)–(3).

gives us access to the quasiparticle thermalization rate and kinetic inductance of MATBG (Fig. 2c, d).

Physical interpretation of the frequency dependence

We now provide a physical interpretation of the rates, Γ_{sw} and Γ_{re} that allows us to connect them to the properties of MATBG. We begin with the switching rate Γ_{sw}. From Eq. (3) we identify the switching rate as $\Gamma_{sw} = R_{bulk}/L_{kin} \propto n_s$ (see additional discussion in Supplementary Information). Assuming that the resistance of normal regions R_{bulk} does not strongly depend on T or bias strength, $\Gamma_{sw}^{-1} \propto L_{kin}$, which allows to probe the superfluid stiffness of MATBG.

Before discussing the thermalization rate of the weak link, we note that for $\omega \gg \Gamma_{sw}$ the AC part of the current does not reach the junction at all: $I_{sc} \approx I_{DC}$. Thus, for $\Gamma_{re} > \Gamma_{sw}$, the kinetic inductance would set the rate for both switching and retrapping. However, as shown in Fig. 4, we have Γ_{re} strictly smaller than Γ_{sw} for all densities (note the different y-axis in Fig. 4a, c), confirming that we can interpret the former as a thermalization rate.

Retrapping rate and thermalization

The equation governing thermalization in the device in Eq. (2) contains two implicit frequency scales: $\gamma \equiv \frac{G_{th}}{C_{el}}$ and $k \equiv \frac{I_J^2 R_J}{C_{el}T_J}$. Importantly, the hysteresis size for DC driving depends on their ratio γ/k (which is proportional to G_{th}, but independent of C_{el}), while the retrapping rate Γ_{re} depends on both, allowing in principle, to determine both scales.

These observations allow for a qualitative discussion of the results (Fig. 4(a,b)) across the MATBG phase diagram. The noticeable peaks in $\Delta I/I_s$, Fig. 4(b), occur near the band insulator (BI) and charge neutrality points (CNP) and indicate a suppressed thermal conductance G_{th}. This can be attributed to a lower density of states near these points compared to other concentrations, expected from previous experiments[32,33] and theoretical analysis[34]. In contrast, Γ_{re} (Fig. 4(a)), which also depends on C_{el} (Fig. 4(a)) shows weaker features at these concentrations, indicating a simultaneous reduction of G_{th} and C_{el}, again consistent with a suppressed density of states. Remarkably, the

minimum of Γ_{re} occurs for densities within the dispersive band. A potential explanation for this behavior is an increased resistance R_J due to the mismatch between flat-band electrons outside the junction and dispersive ones within it. Deeper into the dispersive band, this effect can be offset by an increased G_{th}.

The quantitative nature of Γ_{re} depends on the particular form of $I_J(T)$; for the square-root model introduced above and $\gamma/k < 1/2$ we obtain an analytical result for the retrapping rate: $\Gamma_{re} = \frac{k\sin\frac{2\pi\gamma}{k}}{2\pi}$. Furthermore, the ratio between DC retrapping current and switching is $I_{re}/I_{sw} = \sqrt{\frac{\gamma}{k}}$ (see Supplementary Information). We stress that the observed I_r and I_s are rather close to one another, which results in γ and k being effectively of the same order of magnitude. For larger values of γ the model predicts an $1/\omega^2$ dependence of the retrapping current under AC bias; therefore the model should not be applicable for $I_{re}/I_{sw} > 1/\sqrt{2}$. However, in the absence of direct measurements of $I_J(T)$, we will use this model to estimate C_{el} and G_{th}.

We observe, across the whole density range, three sets of values of Γ_{re}: 0.5 MHz, 1 MHz and 1.5 MHz, corresponding to the chemical potential of the link tuned to the dispersive band, lower flat band and upper flat band, respectively. The change in the hysteresis width, Fig. 4(b) is relatively smaller. Using the analytical formula given above, we can estimate for $\Delta I/I_{sw} \approx 0.5$ that $\gamma \approx 0.8$–2.3 MHz. Reference[22], where laser-mediated heating of a MATBG sample allows for the extraction of the same quantity, reports a value of $\gamma \approx 2$ MHz. The fact that such different methods for extracting the thermalization rate agree on the obtained value strengthens both of them as reliable characterization tools.

This result already provides an important insight into the low-temperature behavior of electron-phonon coupling in MATBG when contrasted with those at higher temperatures. In particular, the cooling rate has been found to be of the order of hundreds of GHz above 5 K with a very weak temperature dependence[23], attributed to effective moiré umklapp scattering[35] (that is related to folding of the acoustic
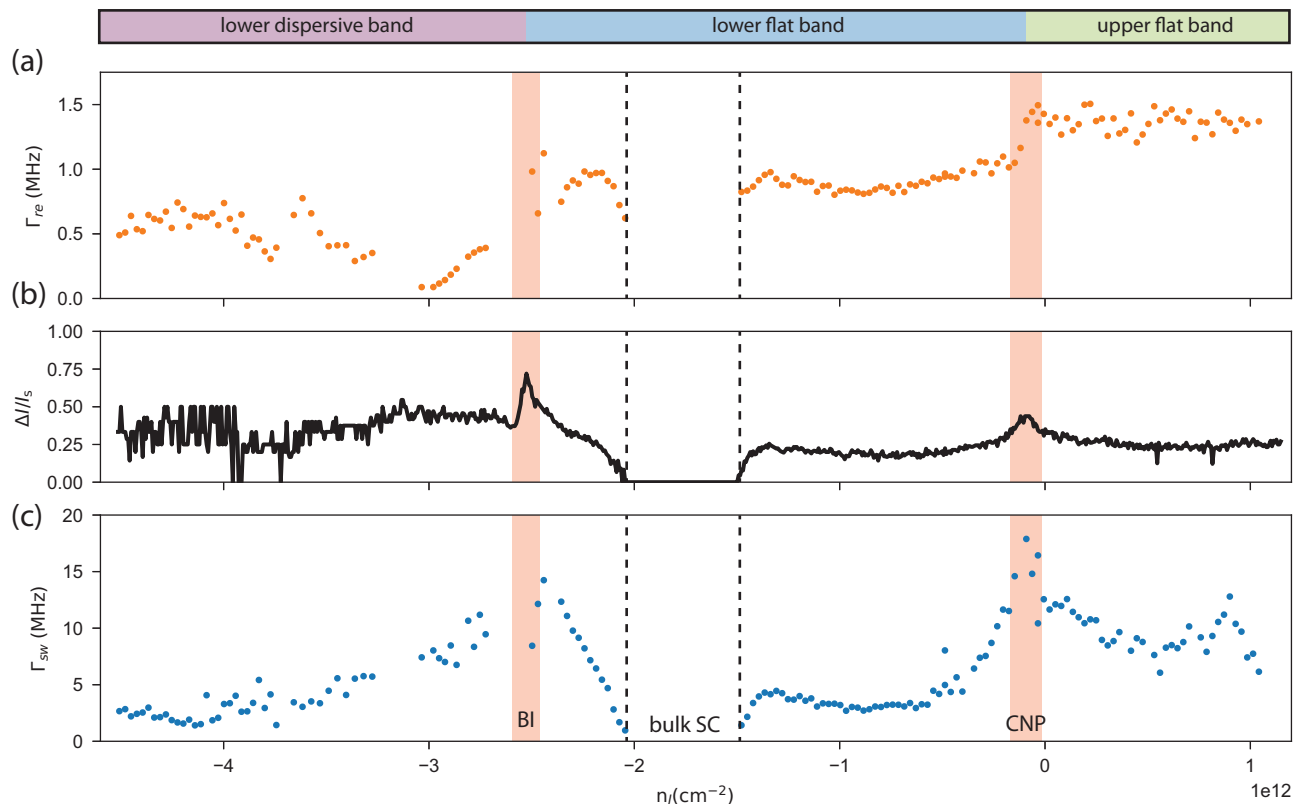
Fig. 4 | Switching and retrapping rates and relative hysteresis across the phase diagram of MATBG. a Retrapping rate as a function of junction density. The region between vertical dashed lines represents the range of densities in which we have a bulk superconductor (SC). **b** Relative hysteresis as a function of junction density. We observe a peak at the charge neutrality point and another one at the band insulator between lower dispersive and flat bands. **c** Switching rate as a function of junction density. The red shaded areas highlight the regions in density where a transition between bands takes place. They correspond to the Charge Neutrality Point (CNP) and Band Insulator (BI).

phonons by the moiré lattice) explaining the linear-in-temperature resistivity[4,10,35]. The strong difference with our result at $T \sim T_J \approx 100$ mK suggests a suppression of the cooling rate much stronger than linear-in-temperature. This result is consistent with electron-phonon scattering at 100 mK being in the Bloch-Gruneisen regime where umklapp scattering is suppressed[35] and resistivity from electron-phonon scattering should follow a stronger power-law dependence on temperature[36]. This excludes electron-phonon scattering as the origin of linear-in-temperature resistance at low temperatures[37].

In the case of superconductivity, the most relevant quantity when discussing electron-phonon coupling is the dimensionless coupling constant, which we note here λ. The temperature relaxation rate at low temperatures is related to the strength of the coupling to acoustic phonons[38–40]. While this coupling does not take the contribution of optical phonons into account, it is expected to be of the same order of magnitude as the full coupling constant[38]. To obtain an estimate we use a Dirac electron model[4,39,40], motivated by the theoretical[34] and experimental evidence[32,33] for their presence in MATBG bands, in particular in the vicinity of CNP (consistent with the peak in $\Delta I/I_s$ discussed above). One finds that $\gamma = \frac{G_{th}}{C_{el}} = \lambda \frac{16\pi^2}{5} \frac{(k_B T_{el})^2}{\hbar^2 s k_F}$, where s is the acoustic phonon velocity. Using $T_{el} \sim T_J \sim 0.1$ K from the extinction temperature of SQUID oscillations[19], $s \approx 20$ km/sec (the value for single-layer graphene[41] is expected to be close to that in MATBG[42]), $k_F = \sqrt{\pi n}$ for $n \sim 1 \times 10^{-12}$ cm^{-2} and $\gamma \sim 1$ MHz we obtain $\lambda \sim 10^{-3}$. Several comments are in order regarding this estimate of λ. We begin by stressing this estimate may not be directly comparable to other transport measurements (e.g., resistivity) as our estimates of λ stem from the electron-phonon cooling rate. While the relation between the way electron-phonon coupling enters the cooling rate, the resistivity, and

the superconducting pairing is established in the Dirac model[4,39,40], it is yet to be determined (and may be different) in the MATBG bands. Moreover, the potential inhomogeneity of the twist angle across the sample may reduce the average thermal relaxation rate, since regions that are away from the magic angle are expected to have lower density of states and thus slower thermal relaxation. Additionally, the above estimate is assuming the system is in the Bloch-Gruneisen regime $T \ll c_s k_F$; it has been however demonstrated[35,43] that the crossover to this regime may be quite different in MATBG than in single-layer graphene and, in particular, it occurs at much lower temperatures. In fact, the strong reduction of the thermal relaxation rate in our experiments with respect to the values at 5 K[23] may present a first demonstration of this crossover occurring in MATBG. We note that this estimate assumes coupling to lowest-energy acoustic phonons only, and does not address optical or any other phonons that are frozen out at the experimental temperatures. Finally, the Dirac model should be applicable only around certain fillings; in our case, a signature of Dirac physics is observed near the CNP in enhanced $\Delta I/I_s$ indicating less efficient heat relaxation due to lower density of states near a Dirac point.

We can further estimate G_{th} and C_{el} taking $I_J \sim I_{exc} \sim 5$ nA, $\Delta V \sim 20$ μV from Fig. 3. The result is $G_{th} \sim 250$ fW/K and $C_{el} \sim 5 \times 10^{19}$ J/K. From the junction area and $n \sim 1 \times 10^{12}$ cm^{-2} one expects above 10^3 electrons, with the usual Sommerfeld expression $C_{el} = \frac{\pi^2}{2} k N \frac{k_B T}{E_F} \sim 10^{-19} \frac{k_B T}{E_F}$ J/K. In usual metals, $\frac{k_B T}{E_F} \ll 1$, while in our case this implies $\frac{k_B T}{E_F} \sim 1$, that may be related to large residual entropy of interacting states of MATBG[44,45]. Both G_{th} and C_{el} are much higher than those expected in monolayer graphene[40], consistent with strongly suppressed bandwidth and electron velocities of MATBG $G \propto v_F^{-2}$, $C \propto v_F$. However, the $\gamma = \frac{G_{th}}{C_{el}}$ we find

in MATBG at $T \approx T_J$ are of the same order as those predicted for monolayer graphene[40].

Switching rate and superfluid stiffness

We now discuss the switching rate Γ_{sw} (Fig. 4c), related to the superfluid stiffness in the bulk of our MATBG device. Importantly, the AC measurements are still performed at a finite DC bias, thus, our measurements reveal the superfluid density at a finite current bias, $n_s(I_{DC}) \approx n_s(I_{sw})$. Since $n_s(I_{sw})$ is a decreasing function of current, the steep increase in Γ_{sw} at the edges of the lower flat band is explained by the decreasing critical current of the junction (Fig. 1 (d)). On the contrary, the decrease of Γ_{sw} for densities in the top flat and dispersive bands, is unexpected - at such low critical currents $n_s(I_{sw}) \approx n_s(0)$ should be density-independent and large. We suggest that this observation can be explained by the kinetic inductance of proximity-induced superconductivity in the junction region. Being very weak, the proximity-induced superfluid has an extremely large kinetic inductance that is in parallel to the smaller one from the bulk TBG, effectively shunting it. Furthermore, since $\Gamma_{sw} \propto R_{bulk}$, changes in the resistance with concentration can also affect its magnitude. In particular, this provides a plausible explanation of the peak of Γ_{sw} near CNP, where the normal-state resistance peaks.

Let us now return to the densities within the lower flat band, where Γ_{sw} is related to the superfluid density of bulk MATBG. The dependence of $\Gamma_{sw} \propto n_s$ as a function of I_{DC}, shown in Fig. 5, gives important information about the nature of the superconducting gap in MATBG. Current biasing a superconductor produces a Doppler shift[46,47] of the quasiparticle bands in a superconductor, see inset of Fig. 5 ($\Delta E = \mathbf{v}_s \times \hbar \mathbf{k}$, where $\mathbf{v}_s$ is the superfluid velocity and $\mathbf{k}$ the quasiparticle momentum). For an isotropic superconductor, depicted in the inset of Fig. 5, this does not affect the quasiparticle occupations until a critical value of bias current is reached. As a result, $n_s(I)$ dependence is highly nonlinear with an abrupt drop close to the critical current[48]. For a highly anisotropic or nodal superconductor, across its nodal axis in real space, the quasiparticle band structure presents cones instead of a gap in density (Fig. 5, inset). A small shift originating from a finite bias current, leads to a finite generation of quasiparticle pairs, thus reducing the superfluid density before breaking down the superconducting condensate. As Fig. 5 shows, the relation between superfluid density and bias current is linear in the case of MATBG in the range $I_{dc} \in [0.6I_c, 0.95I_c]$. This result is inconsistent with the behavior expected of an isotropic superconducting gap, ruling in favor of a highly anisotropic or nodal pairing state in MATBG.

Discussion

In conclusion, we have developed a method for characterizing electron dynamics in twisted bilayer graphene by combining electrostatic and radiofrequency current bias of an electrically-defined Josephson junction. This has resulted in a study of out-of-equilibrium dynamical properties of electrons at cryogenic temperatures in MATBG. Our results demonstrate the presence of two distinct characteristic timescales guiding the dynamics of electrons, attributed to the thermalization of electrons and the kinetic inductance of the superconducting condensate, respectively. A phenomenological model, capturing these processes, is found to describe the data well and allows to relate the measurement outcomes to the physical properties of the electrons in the material for a wide range of densities. In particular, we discuss the estimates for electron-phonon coupling (that may have bearing on theories of superconductivity[4-7] or strange metal[36,37]), specific heat and superfluid density. The current bias dependence of the deduced superfluid stiffness points towards the superconducting gap of the material being anisotropic. The technique we developed in this work can be applied to a wide range of gate-tunable superconducting 2D materials, introducing a general way to access important
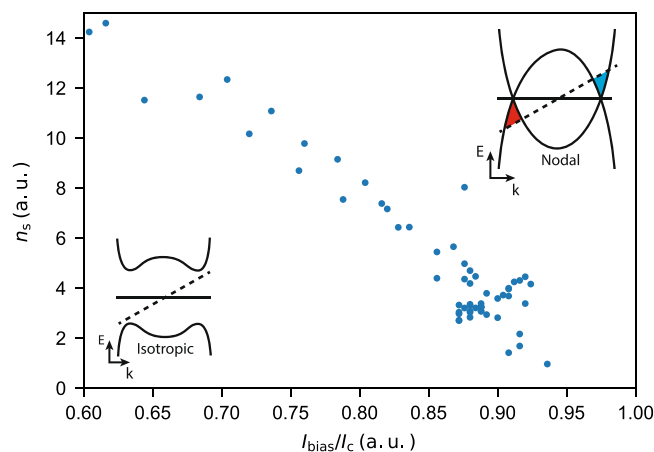

Fig. 5 | Superconducting stiffness in arbitrary units as a function of bias current to critical current ratio. Inset, bottom left: Schematics of Bogoliubov-de Gennes quasiparticle band structure of a superconductor with isotropic gap. The solid straight line represents the Fermi energy at zero current bias. The dashed line represents the Fermi energy at a non-zero current bias. Inset, top right: Schematics of quasiparticle band structure of a superconductor with anisotropic gap. The red and blue areas represent respectively the hole and electron pockets that form at the band edges under a finite current bias.

thermodynamic quantities, such as specific heat and superfluid stiffness. In addition to being a valuable addition to experimental probes of 2D materials, we demonstrated a controllable driving of a correlated electronic system, opening the path to the realization of out of equilibrium states of electrons.

While writing this manuscript the authors became aware of two works where, by different experimental means, some of the quantities studied in this work are also probed[49,50].

Methods

Fabrication details and measurement setup

To fabricate the device, we begin by assembling a so called 'stack' of two dimensional materials. Such flakes are exfoliated mechanically using a micro manipulator, polydimethylsiloxane/polycarbonate stamps, a moving stage and an optical microscope. The stack consists of a bottom layer of few-layer graphite, which is used as a global back-gate, 24 nm-thick hexagonal boron nitride (hBN), the magic angle graphene, and hBN again, this time with a thickness of 27 nm. The twisting and stacking are performed following the standard procedures of the field, with a cutting step of the graphene flake[51]. The graphene-cutting step is performed with a tungsten needle with a tip diameter of $2.5\,\mu m$. Once the stack is in place we move on to the lithography phase of the fabrication process. Gold contacts are defined by a combination of electron-beam lithography, reactive ion etching and electron-beam evaporation. We use chromium as adhesion layer for the gold (10/70 nm). Top gates are defined by electron-beam lithography and evaporation. The graphene is finally etched to define the mesa. A layer of aluminium oxide is deposited through atomic layer deposition. Finally, we define another layer of local gold gates with a chromium adhesion layer (10/110 nm). As a last remark, the device used for this work is the same one as the one presented in reference[18].

In this work, there are however two modifications with respect to the setup of the aforementioned reference. The first one is that the AC bias is not sent to the central gate but to one of the leads, using a bias T to be able to send both AC and DC signals to the same contact. The other difference is that, because for the AC measurements we present in this study we need a higher degree of precision than for the ones presented in reference[18], we must ensure that the AC amplitude reaching the device is neither frequency-dependent nor sample-

resistance-dependent. The details of such procedure are given in the following section.

Radiofrequency biasing

When applying a radiofrequency bias to our junction two different aspects must be taken into account. The first one is the evolution of the amplitude as a function of its frequency. Indeed, having a frequency-dependent amplitude reaching our junction would make it impossible to disentangle such effects from the physical mechanisms taking place at the junction level. We performed simulations of our circuit using the software *LTspice* and obtain an evolution in amplitude of our radio-frequency bias reaching the junction of less than 5%, for frequencies ranging from 100 kHz to 100 MHz. We thus conclude that, in comparison to the experimental results, these effects can be neglected.

Because the junction changes its state during the acquisition of an I/V trace, we must also ensure that the change in resistance triggered by the RF biasing does not significantly affect the AC current flowing through the device. In order to achieve that, we place a 100 kΩ resistor in series between the RF feed line and the device. Like for the previous effect, this leads to a variation in AC amplitude reaching the device of the order of a few percents across the whole resistivity range of the device. We thus can also neglect this effect taking into account the precision of the claims made in our analysis. Supplementary Fig. 1 shows a schematics of the electronics set-up. We neglect in this schematics the capacitances from the MATBG to the gold or graphite gate electrodes because they are smaller than 30 fF[18]. They thus present, at the frequencies at which we bias our sample (up to 100 MHz), an impedance orders of magnitude higher than any other impedance in the set-up.

Data availability

The data that support the findings of this study, together with the code for plotting the figures, is available online through the ETH Research Collection at https://doi.org/10.3929/ethz-b-000722186.

References

1. Cao, Y. et al. Unconventional superconductivity in magic-angle graphene superlattices. *Nature* **556**, 43–50 (2018).
2. Cao, Y. et al. Correlated insulator behaviour at half-filling in magic-angle graphene superlattices. *Nature* **556**, 80–84 (2018).
3. Lu, X. et al. Superconductors, orbital magnets and correlated states in magic-angle bilayer graphene. *Nature* **574**, 653–657 (2019).
4. Wu, F., Hwang, E. & Das Sarma, S. Phonon-induced giant linear-in-*t* resistivity in magic angle twisted bilayer graphene: Ordinary strangeness and exotic superconductivity. *Phys. Rev. B* **99**, 165112 (2019).
5. Lian, B., Wang, Z. & Bernevig, B. A. Twisted bilayer graphene: A phonon-driven superconductor. *Phys. Rev. Lett.* **122**, 257002 (2019).
6. Wu, F., MacDonald, A. H. & Martin, I. Theory of phonon-mediated superconductivity in twisted bilayer graphene. *Phys. Rev. Lett.* **121**, 257001 (2018).
7. Kennes, D. M., Lischner, J. & Karrasch, C. Strong correlations and d + id superconductivity in twisted bilayer graphene. *Phys. Rev. B* **98**, 241407 (2018).
8. Oh, M. et al. Evidence for unconventional superconductivity in twisted bilayer graphene. *Nature* **600**, 240–245 (2021).
9. Kim, H. et al. Evidence for unconventional superconductivity in twisted trilayer graphene. *Nature* **606**, 494–500 (2022).
10. Polshyn, H. et al. Large linear-in-temperature resistivity in twisted bilayer graphene. *Nat. Phys.* **15**, 1011–1016 (2019).
11. Zhou, H. et al. Isospin magnetism and spin-polarized superconductivity in bernal bilayer graphene. *Science* **375**, 774–778 (2022).
12. Jindal, A. et al. Coupled ferroelectricity and superconductivity in bilayer td − mote$_2$. *Nature* **613**, 48–52 (2023).
13. Xia, Y. et al. Superconductivity in twisted bilayer wse2. *Nature* **637**, 1–6 (2024).
14. Han, T. et al. Signatures of chiral superconductivity in rhombohedral graphene. Preprint at https://arxiv.org/abs/2408.15233 (2024).
15. Wollman, D. A., Van Harlingen, D. J., Lee, W. C., Ginsberg, D. M. & Leggett, A. J. Experimental determination of the superconducting pairing state in ybco from the phase coherence of ybco-pb dc squids. *Phys. Rev. Lett.* **71**, 2134–2137 (1993).
16. López-Núñez, D. et al. Magnetic penetration depth of aluminum thin films. Preprint at https://arxiv.org/abs/2311.14119 (2023).
17. Chiodi, F., Aprili, M. & Reulet, B. Evidence for two time scales in long sns junctions. *Phys. Rev. Lett.* **103**, 177002 (2009).
18. de Vries, F. K. et al. Gate-defined Josephson junctions in magic-angle twisted bilayer graphene. *Nat. Nanotechnol.* **16**, 760–763 (2021).
19. Portolés, E. et al. A tunable monolithic squid in twisted bilayer graphene. *Nat. Nanotechnol.* **17**, 1159–1164 (2022).
20. Díez-Mérida, J. et al. Symmetry-broken josephson junctions and superconducting diodes in magic-angle twisted bilayer graphene. *Nat. Commun.* **14**, 2396 (2023).
21. Rodan-Legrain, D. et al. Highly tunable junctions and non-local josephson effect in magic-angle graphene tunnelling devices. *Nat. Nanotechnol.* **16**, 769–775 (2021).
22. Di Battista, G. et al. Revealing the thermal properties of superconducting magic-angle twisted bilayer graphene. *Nano Lett.* **22**, 6465–6470 (2022).
23. Mehew, J. D. et al. Ultrafast umklapp-assisted electron-phonon cooling in magic-angle twisted bilayer graphene. *Sci. Adv.* **10**, eadj1361 (2024).
24. Tinkham, M. *Introduction to superconductivity* (Dover, 2004).
25. Blonder, G. E., Tinkham, M. & Klapwijk, T. M. Transition from metallic to tunneling regimes in superconducting microconstrictions: Excess current, charge imbalance, and supercurrent conversion. *Phys. Rev. B* **25**, 4515–4532 (1982).
26. Courtois, H., Meschke, M., Peltonen, J. T. & Pekola, J. P. Origin of hysteresis in a proximity josephson junction. *Phys. Rev. Lett.* **101**, 067002 (2008).
27. Fong, K. C. & Schwab, K. C. Ultrasensitive and wide-bandwidth thermal measurements of graphene at low temperatures. *Phys. Rev. X* **2**, 031006 (2012).
28. Angers, L. et al. Proximity dc squids in the long-junction limit. *Phys. Rev. B* **77**, 165408 (2008).
29. Fong, K. C. et al. Measurement of the electronic thermal conductance channels and heat capacity of graphene at low temperature. *Phys. Rev. X* **3**, 041008 (2013).
30. Seifert, P. et al. Magic-angle bilayer graphene nanocalorimeters: Toward broadband, energy-resolving single photon detection. *Nano Lett.* **20**, 3459–3464 (2020).
31. Uri, A. et al. Mapping the twist-angle disorder and landau levels in magic-angle graphene. *Nature* **581**, 47–52 (2020).
32. Zondiner, U. et al. Cascade of phase transitions and dirac revivals in magic-angle graphene. *Nature* **582**, 203–208 (2020).
33. Tian, H. et al. Evidence for dirac flat band superconductivity enabled by quantum geometry. *Nature* **614**, 440–444 (2023).
34. Carr, S., Fang, S., Zhu, Z. & Kaxiras, E. Exact continuum model for low-energy electronic states of twisted bilayer graphene. *Phys. Rev. Res.* **1**, 013001 (2019).
35. Ishizuka, H., Fahimniya, A., Guinea, F. & Levitov, L. Purcell-like enhancement of electron–phonon interactions in long-period superlattices: Linear-temperature resistivity and cooling power. *Nano Lett.* **21**, 7465–7471 (2021).
36. Das Sarma, S. & Wu, F. Strange metallicity of moiré twisted bilayer graphene. *Phys. Rev. Res.* **4**, 033061 (2022).
37. Jaoui, A. et al. Quantum critical behaviour in magic-angle twisted bilayer graphene. *Nat. Phys.* **18**, 633–638 (2022).

38. Allen, P. B. Theory of thermal relaxation of electrons in metals. *Phys. Rev. Lett.* **59**, 1460–1463 (1987).

39. Viljas, J. K. & Heikkilä, T. T. Electron-phonon heat transfer in monolayer and bilayer graphene. *Phys. Rev. B* **81**, 245404 (2010).

40. Walsh, E. D. et al. Graphene-based josephson-junction single-photon detector. *Phys. Rev. Appl.* **8**, 024022 (2017).

41. Cong, X. et al. Probing the acoustic phonon dispersion and sound velocity of graphene by raman spectroscopy. *Carbon* **149**, 19–24 (2019).

42. Koshino, M. & Son, Y.-W. Moiré phonons in twisted bilayer graphene. *Phys. Rev. B* **100**, 075416 (2019).

43. Davis, S. M., Wu, F. & Das Sarma, S. Acoustic phonon contribution to the resistivity of twisted bilayer graphene. *Phys. Rev. B* **107**, 235155 (2023).

44. Rozen, A. et al. Entropic evidence for a pomeranchuk effect in magic-angle graphene. *Nature* **592**, 214–219 (2021).

45. The proximity effect through a junction is related to its excess current. We discuss such relation in our device in Supplementary Material.

46. Yip, S. K. & Sauls, J. A. Nonlinear meissner effect in cuo super-conductors. *Phys. Rev. Lett.* **69**, 2264–2267 (1992).

47. Volovik, G. E. Superconductivity with lines of gap nodes: density of states in the vortex. *JETP Lett.* **58**, 457 (1993).

48. Clem, J. R. & Kogan, V. G. Kinetic impedance and depairing in thin and narrow superconducting films. *Phys. Rev. B* **86**, 174521 (2012).

49. Tanaka, M. et al. Superfluid stiffness of magic-angle twisted bilayer graphene. *Nature* **638**, 99–105 (2025).

50. Banerjee, A. et al. Superfluid stiffness of twisted trilayer graphene superconductors. *Nature* **638**, 93–98 (2025).

51. Kim, K. et al. van der waals heterostructures with high accuracy rotational alignment. *Nano Lett.* **16**, 1989–1995 (2016).

Author contributions
P.R. and E.P. fabricated the device. F.K.d.V., E.P., and P.R. characterized the device. T.T. and K.W. supplied the hBN crystals. E.P. and M.P. performed the measurements for this experiment. E.P., P.A.V., M.P., M.T., and Y.K. analyzed the data with input from A.M-T, A.O.D., and G.Z.; P.A.V. developed the theoretical model and performed the numerical and analytical calculations. K.E., T.I., and E.P. conceived and designed the experiment. J.H.P., T.I., and K.E. supervised the project. E.P. and P.A.V. wrote the manuscript with comments from all authors.

Competing interests
The authors declare no competing interests.

Additional information
Supplementary information The online version contains supplementary material available at https://doi.org/10.1038/s41467-025-58325-0.

Correspondence and requests for materials should be addressed to Elías Portolés or Pavel A. Volkov.

Peer review information *Nature Communications* thanks Jianpeng Liu, and the other, anonymous, reviewer for their contribution to the peer review of this work. A peer review file is available.

Reprints and permissions information is available at http://www.nature.com/reprints

Publisher's note Springer Nature remains neutral with regard to jurisdictional claims in published maps and institutional affiliations.